

Article

# Comparative Aerodynamic Performance Analysis of Camber Morphing and Conventional Airfoils

Tuba Majid and Bruce W. Jo \* 

Advanced Dynamics Mechatronics and Collaborative Robotics (ADAMS) Laboratory, Department of Mechanical Engineering, State University of New York (SUNY), Stony Brook University, Incheon 406840, Korea; tuba.majid@stonybrook.edu

\* Correspondence: bruce.jo@stonybrook.edu

**Abstract:** This paper aims to numerically validate the aerodynamic performance and benefits of variable camber rate morphing wings, by comparing them to conventional ones with plain flaps, when deflection angles vary, assessing their D reduction or L/D improvement. Many morphing-related research works mainly focus on the design of morphing mechanisms using smart materials, and innovative mechanism designs through materials and structure advancements. However, the foundational work that establishes the motivation of morphing technology development has been overlooked in most research works. All things considered, this paper starts with the verification of the numerical model used for the aerodynamic performance analysis and then conducts the aerodynamic performance analysis of (1) variable camber rate in morphing wings and (2) variable deflection angles in conventional wings. Finally, we find matching pairs for a direct comparison to validate the effectiveness of morphing wings. As a result, we validate that variable camber morphing wings, equivalent to conventional wings with varying flap deflection angles, are improved by at least 1.7% in their L/D ratio, and up to 18.7% in their angle of attack, with  $\alpha = 8^\circ$  at a 3% camber morphing rate. Overall, in the entire range of  $\alpha$ , which conceptualizes aircrafts mission planning for operation, camber morphing wings are superior in D, L/D, and their improvement rate over conventional ones. By providing the improvement rates in L/D, this paper numerically evaluates and validates the efficiency of camber morphing aircraft, the most important aspect of aircraft operation, as well as the agility and manoeuvrability, compared to conventional wing aircraft.

**Keywords:** camber morphing; flaps; airfoil configurations; low Reynolds number; aerodynamic performance; lift-to-drag ratio; lift; drag; comparative analysis



**Citation:** Majid, T.; Jo, B.W. Comparative Aerodynamic Performance Analysis of Camber Morphing and Conventional Airfoils. *Appl. Sci.* **2021**, *11*, 10663. <https://doi.org/10.3390/app112210663>

Academic Editor: Wei Huang

Received: 24 October 2021

Accepted: 9 November 2021

Published: 12 November 2021

**Publisher's Note:** MDPI stays neutral with regard to jurisdictional claims in published maps and institutional affiliations.



**Copyright:** © 2021 by the authors. Licensee MDPI, Basel, Switzerland. This article is an open access article distributed under the terms and conditions of the Creative Commons Attribution (CC BY) license (<https://creativecommons.org/licenses/by/4.0/>).

## 1. Introduction

The term morphing is from “metamorphosis” and means a change of the form, or nature of a thing, or a person, into a completely different one by natural or supernatural means [1]. In the aerospace and aviation industry, morphing technologies have been adopted to aim for enhanced flight performance by adjusting the aircraft’s structure, particularly wing shapes, to optimize flight states and conditions by matching with the corresponding flight mode. If the concept of morphing in wings is broadly defined, control surfaces in conventional aircrafts could also be included; however, morphing wings typically refer to active, continuous, and more substantial changes in the wing structures from its initial design stage. Whereas conventional wing aircrafts manoeuvre and change their flight dynamics by changing the deflection angles of various control surfaces such as flaps, aileron, elevator, rudder, and so on, as well as the wing area by expanding chord lengths, the concept of morphing wing aircraft relies on irregular changes of wing structures including changes in airfoil thickness, camber, span lengths, sweep angles, span bend, and twist as depicted in Figure 1 [2].

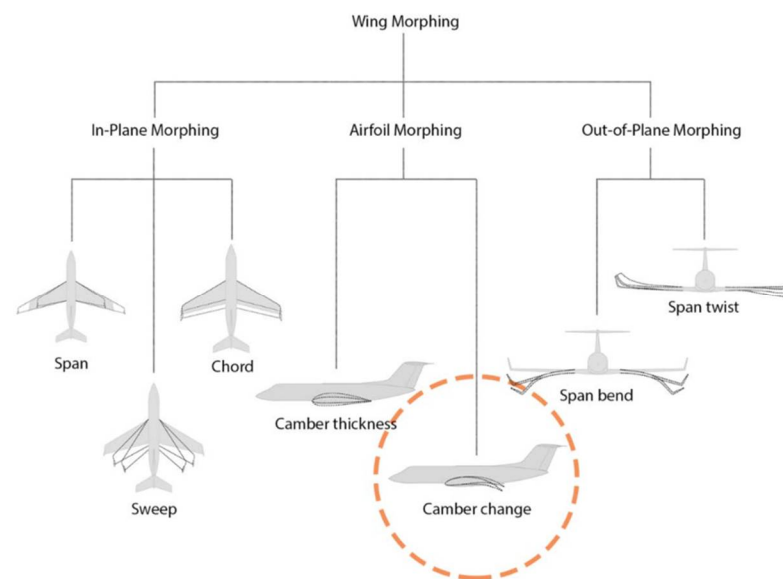


**Figure 1.** Categories of morphing types in fixed-wing aircraft.

A major and well-acclaimed aerodynamic benefit of a morphing structure is from its potential to create unusual and substantial shape changes that could satisfy various flight conditions, which a conventional aircraft could not generate. On the basis of these changes one can expect to implement, design, and test morphing wings and equip aircrafts to optimize their flight condition, which could also imply that the morphing aircraft could fly longer, consume less fuel, be more energy effective, and more agile than the same weight conventional ones. One of the important aerodynamic parameters linked to fuel consumption or energy saving could be  $D$ , the drag forces exerted on the aircraft during flight, so a reduction in  $D$  should preserve fuel. The aforementioned morphing wings can potentially initiate a larger envelope in flight performance that enables extra residual flight modes of better or smaller  $D$  by continuously altering wing shapes.

The different types of morphing along with the geometric parameter that is modified to create the morphing are shown in Figure 1, and amongst them, this paper explores camber change or camber rate morphing. The camber rate of an airfoil (denoted by the first digit in the four-digit NACA airfoil series) describes the convexity of an airfoil between its leading and trailing edges. Continuously changing the camber has benefits in terms of  $L$  distribution, improved manoeuvrability, improved  $L/D$ , expanded flight envelope, and tactical capabilities [1]. A conventional wing with deflecting control surfaces and a morphing wing with varying camber is shown in Figure 2.

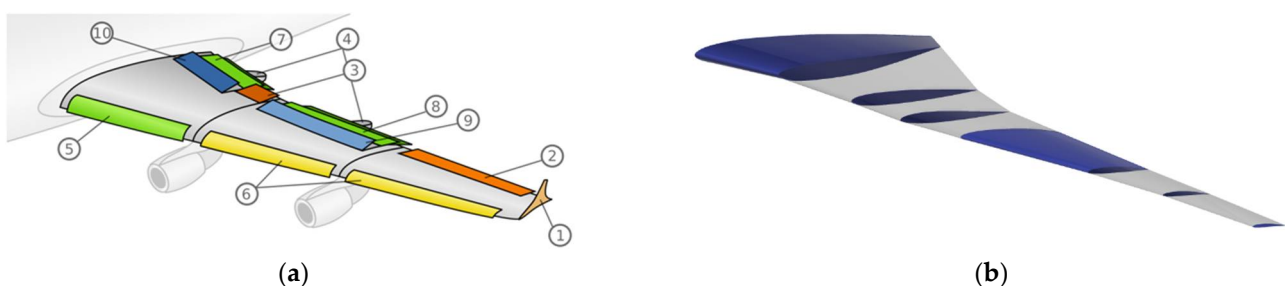


**Figure 2.** A conventional wing with control surfaces [3] (a) and a camber morphing wing (b). Control Surfaces: (1) winglet, (2) low-speed aileron, (3) high-speed aileron, (4) flap track fairing, (5) Kruger flaps, (6) slats, (7) three-slotted inner flaps, (8) three-slotted outer flaps, (9) spoilers, (10) spoilers-air brakes.

Most of the morphing wing research works focus on either the design and implementation of morphing concepts using selected materials and structures [4–11], or the

analysis of the structural and aerodynamic performance of suggested morphing concepts and their mechanisms [12–15]. Researchers have developed camber morphing mechanisms using smart materials [16–18], corrugated structures [19], multi-unit rib structures [20], vertically slitted rib structures [21], truss elements and runners [22], pressure-actuated cellular structures [23,24], bio-inspired FishBAC structures [25], monolithic compliant mechanisms [26], or combined form [27] to introduce and validate their effectively working models and design implementation. Some morphing wing design implementations were even validated with an effectively flown test model [27–31]. Probably one of the most similar works done by [32] took the CFD study of morphing wings and compared them with an analytical solution to validate the effectiveness of the suggested numerical models and approaches. It is noted that over the last decades, significant and meaningful papers and projects have been written and performed from various different aspects [33–37]. However, the ultimate aerodynamic benefits of using morphing wings (in terms of its aerodynamic efficiency,  $L/D$ , compared to different configurations of conventional wings with control surfaces deflected to different angles)—probably one of the most important aspects and foundational milestones for designing and analysing morphing wings—has not been addressed or quantitatively validated so far in the literature.

## 2. Problem Statement

Research works on the computational performance of morphing technology mainly focus on the aerodynamic analysis of targeted configurations of certain morphing styles and their mechanisms [38,39] only, or additionally, on the morphing concept's degree of deformation and power consumption [40,41]. The main objective of this work is to clarify the actual and quantitative benefits of morphing wings regarding their  $D$  reduction by comparison of various camber morphing rates with different configuration of conventional wings generated for various flap deflection angles.

It is important to understand and validate the benefits of morphing wings, and the methodology authors use in this paper is through a numerical approach employing a high-fidelity CFD software ANSYS Fluent. Through a rigorous analysis, the aerodynamic forces are computed over a range of  $\alpha$  for both the morphed and deflected configurations by varying the maximum camber rate for the morphing cases and varying the flap deflection angle for the deflecting cases. The computational methodology is presented in Section 2, along with the validation study, details about the ANSYS Fluent setup, grid generation, and the geometries of the airfoil configurations. The computed results are discussed in Section 3, where the authors verify any improvement of  $L/D$  in morphed configurations, for configurations matched in  $L$  between morphing and conventional wing pairs. The  $L$  profiles are matched to establish the same conditions for comparison while  $\alpha$  is varied and  $D$  analysed and compared. Lastly, the conclusions are given in Section 4. It is of interest to evaluate the actual benefits of camber morphing wings in terms of their  $L/D$  improvement, indicative of enhanced sustainability for more practical aspects of real-world applications, and mission planning along an assigned trajectory.

## 3. Methodology

### 3.1. Computational Method and Verification

The fluid flow around the 2D airfoils was simulated using CFD software ANSYS Fluent to predict the aerodynamic forces:  $L$  and  $D$ . The adopted numerical technique is a finite volume discretization method, with a pressure-based solver to solve the Reynolds-averaged version of these equations, coupled with a one-equation Spalart–Allmaras (S-A) turbulence model [42] to compute the Reynolds stresses in the Reynolds-averaged Navier–Stokes (RANS) equations. The calculations depend on computing the S-A working variable, which obeys the following transport equation:

$$\frac{D\tilde{v}}{Dt} = c_{b12}[1 - f_{t2}]\tilde{S}\tilde{v} + \frac{1}{\sigma} \left[ \nabla \cdot \left( (v + \tilde{v}) \nabla \tilde{v} \right) + c_{b2} (\nabla \tilde{v})^2 \right] - \left[ c_{w1} f_w - \frac{c_{b1}}{\kappa^2} \right] \left[ \frac{(\tilde{v})}{d} \right]^2 + f_{t1} \Delta U^2 \quad (1)$$

A C-type unstructured mesh was used in the fluid domain, with a C segment radius of 7.5 m and a rectangular block measuring 16.5 m by 15 m. These dimensions were set based on the length recommended for simulating the flow around an airfoil of chord length 1 m [43]. Then, 25 inflation layers were generated around the airfoil, with a growth rate of 1.1 to resolve the viscous sublayer in the near-wall region and the first layer thickness,  $y$ , computed from the given equation [44]:

$$y = \frac{y^+ \mu}{\rho \sqrt{\frac{1}{2} C_f v^2}} \quad (2)$$

where:

$$C_f = 0.058 Re^{-0.2} \quad (3)$$

The values for the  $\rho$  and  $v$  used in the equation correspond to the  $Re$  the flow was being simulated for, and the first layer thickness calculated to maintain  $y^+$  values of less than 1 at the wall. It was confirmed that the  $y^+$  values at the airfoil boundary in all our setups were in a range of 1 to less than 1, as shown in Figure 3, which also shows the computational domain, and the grid from one of our setups.

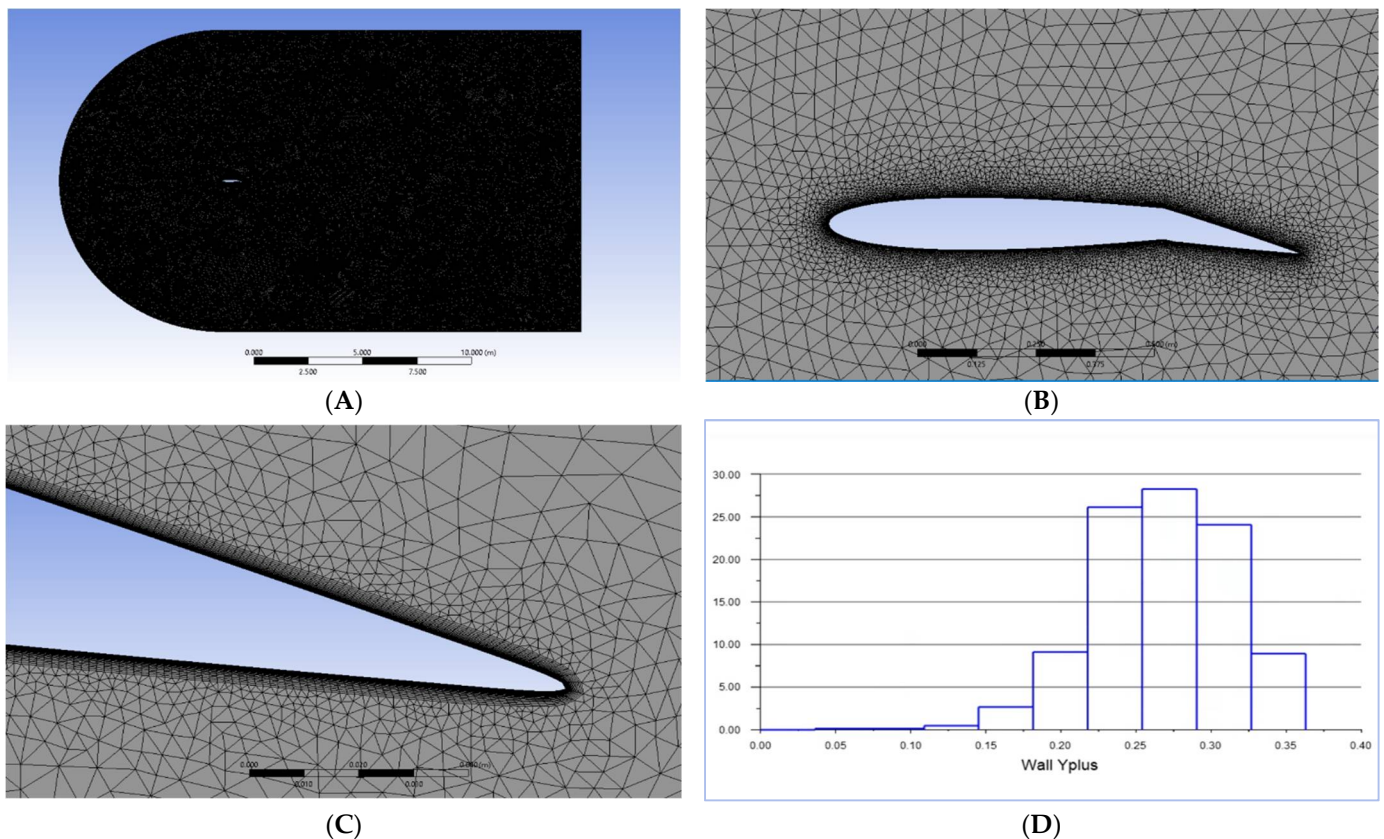


**Figure 3.** (A) Computational domain; (B) mesh near the airfoil; (C) inflation layers around the airfoil; (D) histogram of airfoil Wall Yplus ( $y^+$ ).

A mesh independence study was conducted as well. A Richardson extrapolation has been adopted to calculate the grid convergence index, and it was confirmed that an index of less than 3% was obtained for the various grids tested. Computational time also plays a role in deciding the mesh element size. The grid comprising 7,060,448 elements

(element size: 0.01 m) was the most refined mesh tested, but as shown in Figure 4, varying the element size and thus the number of cells, shows only minor changes in the values of  $C_D$  obtained from the simulations. Therefore, the element size was adjusted to 0.05 m for the rest of the study, which would generate around 350,000 elements for the geometric configurations tested.

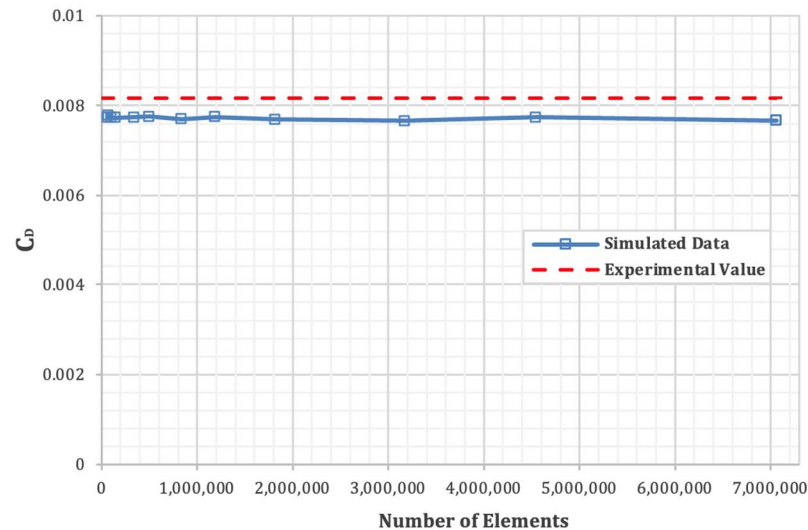


**Figure 4.** Mesh independence study (NACA 0012 airfoil,  $Re = 6$  million,  $\alpha = 0^\circ$ ).

The values for the flow properties such as the freestream velocity and the fluid density, and parameters of viscosity such as  $\mu$ , input in the setup, were set to correspond to the  $Re$  the flow was being simulated for. A  $Re$  of 76,630 was chosen for this study since we compare the performance of a camber morphing and a conventional airfoil with a plain flap, at actual flight conditions, of a small UAV or MAV. A velocity-based inlet and a pressure-based outlet were used as the boundary conditions with a no-slip condition imposed on the airfoil surface. In the solution methods, a coupled scheme was found to be more accurate and compatible with our unstructured mesh, and a convergence criterion of  $10^{-6}$  was set for all computed residuals.

In the ANSYS Fluent setup, we set the  $\alpha$  as a parameter and compute the corresponding  $L$  and  $D$  values. With each setup being a parametric study of the respective morphing or conventional airfoil cases, over a range of  $\alpha$  from  $0^\circ$  to  $15^\circ$ , the  $L$  and  $D$  would need to be computed with respect to the  $\alpha$  the flow was being simulated for. However, ANSYS Fluent does not have the option to set the  $L$  and  $D$ 's direction vector as a parameter so the normal  $x$  and  $y$  components,  $F_x$  and  $F_y$ , were generated using ANSYS Fluent and those values were transformed using a rotation matrix to compute the  $L$  and  $D$ . The  $L$ ,  $D$  in the matrix corresponds to the  $\alpha$ , and the equations used are stated below:

$$\begin{bmatrix} L \\ D \end{bmatrix} = \begin{bmatrix} \cos \alpha & \sin \alpha \\ -\sin \alpha & \cos \alpha \end{bmatrix} \begin{bmatrix} F_x \\ F_y \end{bmatrix} \quad (4)$$

To verify the reliability, the flow was simulated around a NACA 0012 airfoil at 6 million  $Re$  and the  $C_L$  and  $C_D$  were computed and compared with the validation case provided by NASA's Langley Research Center [45,46] as shown in in Figure 5. Two different turbulence models, (1) Spalart–Allmaras ( $S-A$ ) and (2)  $k$ - $\omega$  with SST ( $k$ - $\omega$ ) were tested. Although both can be seen to be in good agreement with the validation cases, the  $S-A$  turbulence model was selected for the aerodynamic simulations as it has good accuracy, comes at a relatively low computational cost, and is recommended for low- $Re$  flow simulations [43].

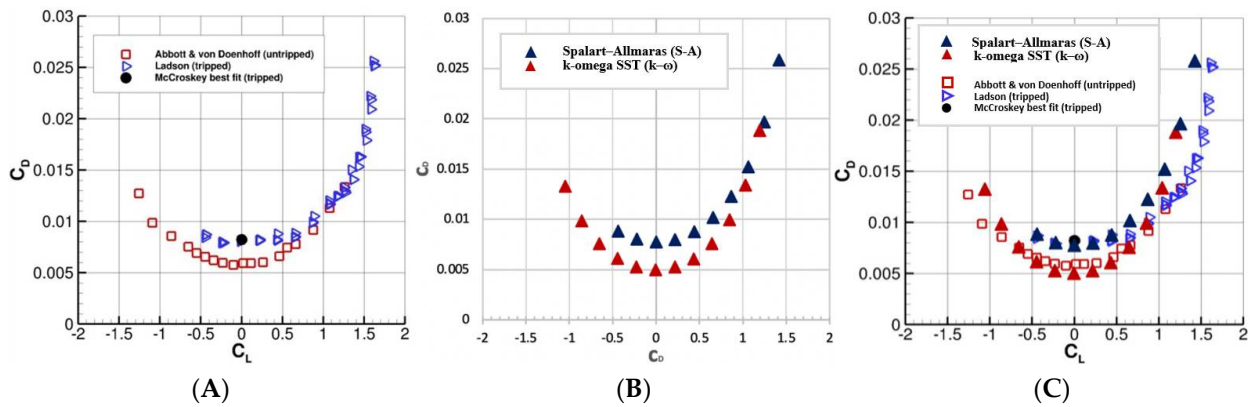


**Figure 5.** CFD setup validation case study results (NACA0012,  $Re = 6$  million). (A) Drag polar based on NASA Langley Research Center validation case data. (B) Drag polar generated using the proposed CFD methodology with 2 different turbulence models. (C) Comparison of simulated results (B) with validation case (A).

### 3.2. Airfoil Geometry Configuration

The airfoil geometry imported into the Design Modeler was designed using the CAD design software Fusion 360, based on the airfoil coordinates generated using a NACA 4-digit airfoil calculator [47]. Figure 6 shows the geometry of a morphing and a conventional airfoil with the indicated baseline (dotted line). For the morphing airfoil cases, the position of maximum camber was fixed at 40% from the leading edge and the first digit of the 4-digit NACA airfoil series varied (the first digit, i.e., the X in NACA X412, denotes the maximum camber rate). For the conventional airfoil case, the flap joint was placed at 70% of the chord length of the NACA 0012 airfoil and the angle rotated clockwise at the joint for the flap deflection angle. The maximum camber rate was varied from 0% to 9% with increment of 1% to generate the morphing airfoil configurations and the flap deflection angle varied in increments of  $0.25^\circ$  from  $0^\circ$  to  $21.5^\circ$  to generate deflecting airfoil configurations. These geometries were then exported in step format to be used in ANSYS Fluent for the numerical analysis.



**Figure 6.** A schematic diagram of (a) a conventional airfoil with a deflecting flap (purple) and (b) a morphing airfoil (yellow).

## 4. Results

CFD simulations were run and the  $C_L$  and  $C_D$  computed for various morphed and deflected airfoil configurations, over a range of  $\alpha$  from  $0^\circ$  to  $15^\circ$ . The plots of the  $C_L$  of different morphed cases are presented in Figure 7 and the deflected cases in Figure 8. For clarity, only those configurations that match the  $L$  profiles of morphing configurations or contribute to the overlapping regions were included in the conventional airfoil  $L$  plots in Figures 8 and 10.

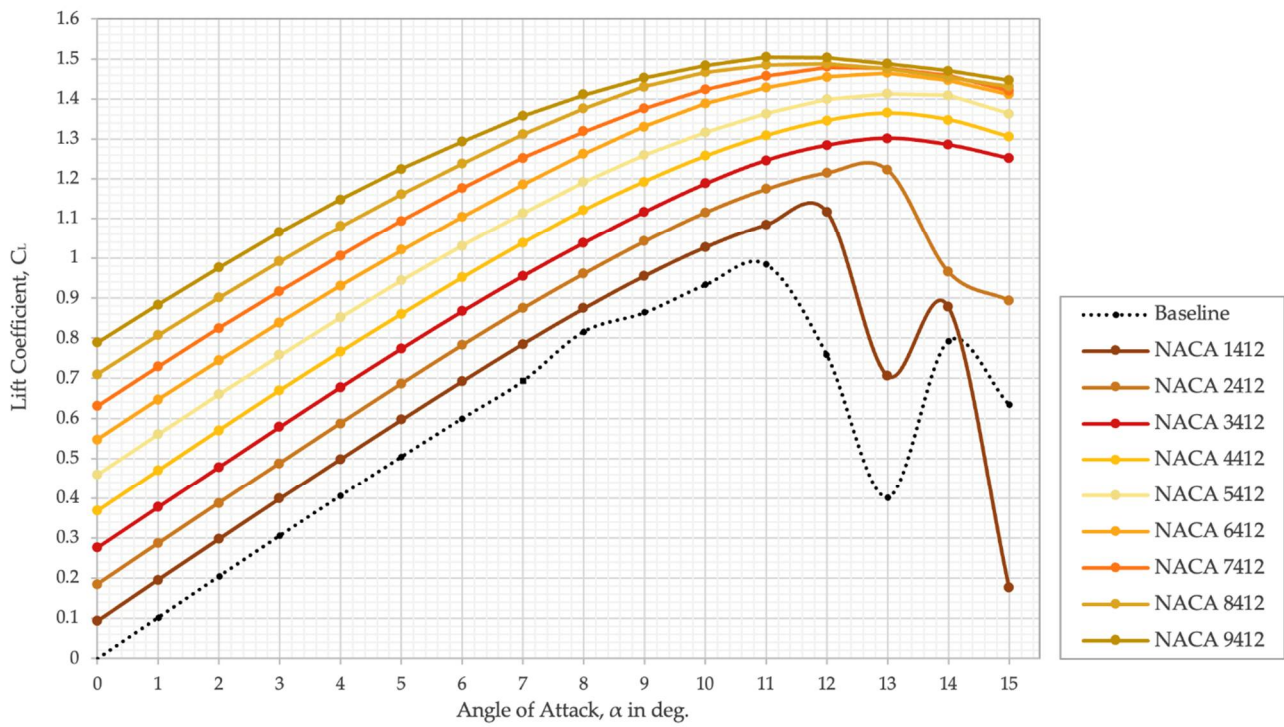


Figure 7. Morphing airfoils  $C_L$  vs.  $\alpha$  varying the maximum camber rate. ( $Re = 76,630$ ).

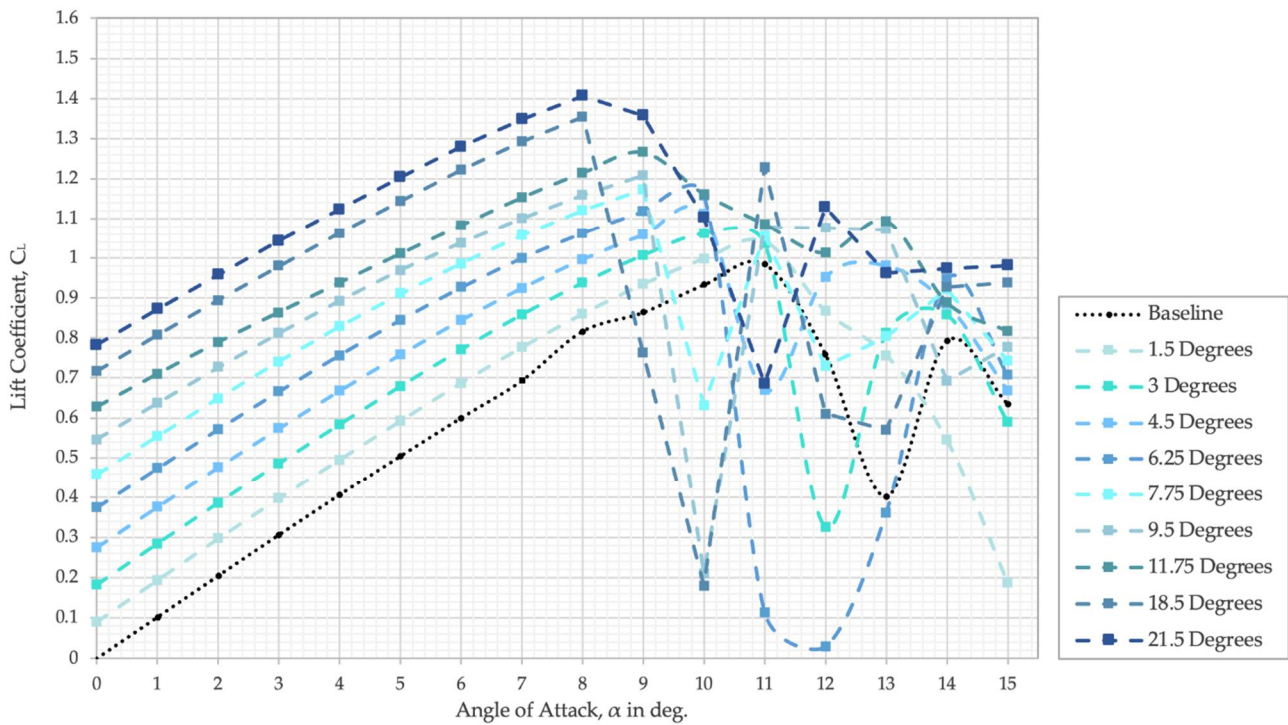


Figure 8. Conventional airfoils  $C_L$  vs.  $\alpha$  varying the flap deflection angle. ( $Re = 76,630$ ).

From Figures 7 and 8, it is noted that morphing airfoils stall starting at a higher  $\alpha$  than the conventional, deflecting airfoils. Typically, the stall region for airfoils in the 50,000–100,000  $Re$  regions is between  $10^\circ$  to  $14^\circ$  [48] and our results confirm that. The approximated stall angles extrapolated from the plots or identified based on the readings are presented in Table 1.

Table 1. Summary of the matching cases.

Matching Cases	Morphing Airfoils		Conventional Airfoils		Overlapping Region
	Maximum Camber Rate (%)	Stall Angle (°)	Flap Deflection Angle (°)	Stall Angle (°)	
Baseline	NACA 0012—0%	11°	0°	11°	All angles
Case 1	NACA 1412—1%	11.8°	1.5°	11°	10 angles
Case 2	NACA 2412—2%	12.6°	3°	10.6°	9 angles
Case 3	NACA 3412—3%	13°	4.5°	10°	7 angles
Case 4	NACA 4412—4%	13°	6.25°	9°	5 angles
Case 5	NACA 5412—5%	13°	7.75°	9°	4 angles
Case 6	NACA 6412—6%	13°	9.5°	9°	3 angles
Case 7	NACA 7412—7%	12°	11.75°	9°	2 angles
Case 8	NACA 8412—8%	12°	18.5°	8°	8 angles
Case 9	NACA 9412—9%	11°	21.5°	8°	9 angles

For the camber morphing, the value of  $\alpha$  at maximum  $L$  increases as the camber rate increases until it reaches a peak at  $\alpha = 13^\circ$  between camber rate of 3% and 6%. However, at 7% and greater (7–9%) rates, the angle starts to decrease, and the maximum  $C_L$  is obtained at  $\alpha < 13^\circ$ . This trend of a decreasing stall angle as the camber rate increases is to be expected since as the camber of the airfoil increases, the geometric change creates a suction peak on the upper surface near the leading edge that leads to an easier onset of boundary layer separation. NACA 6412 airfoil stalls at around  $13^\circ$  but a 9% cambered airfoil—NACA 9412—stalls at around  $11^\circ$ . Pressure contours of 6% and 9% morphed airfoils at their respective stall angles are shown in Figure 9 and the contours for both configurations are very similar, which is consistent with the trend and the lift values of Figure 7, where the amount of lift generated by these configurations is around a similar range.

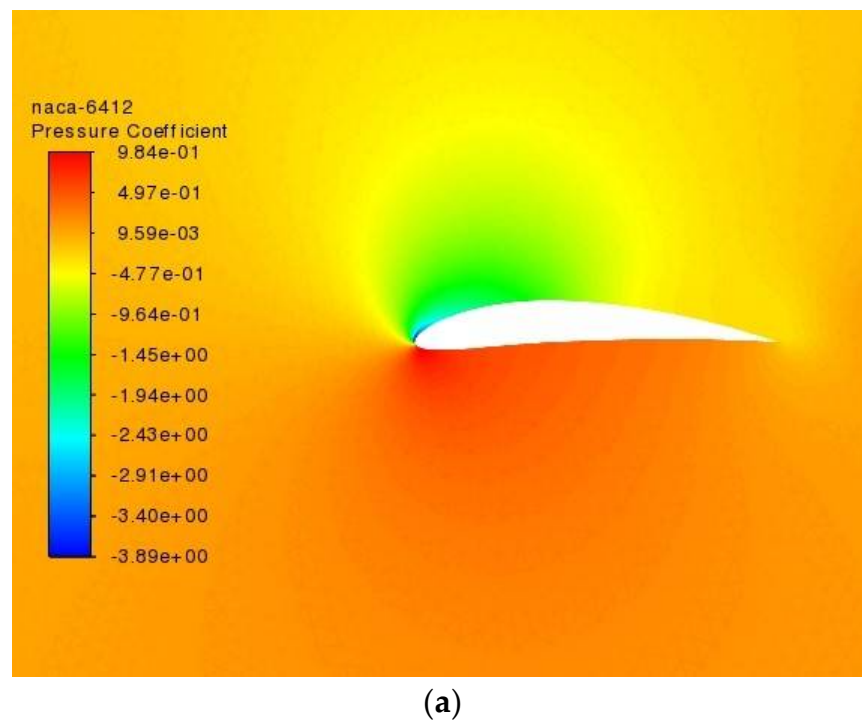
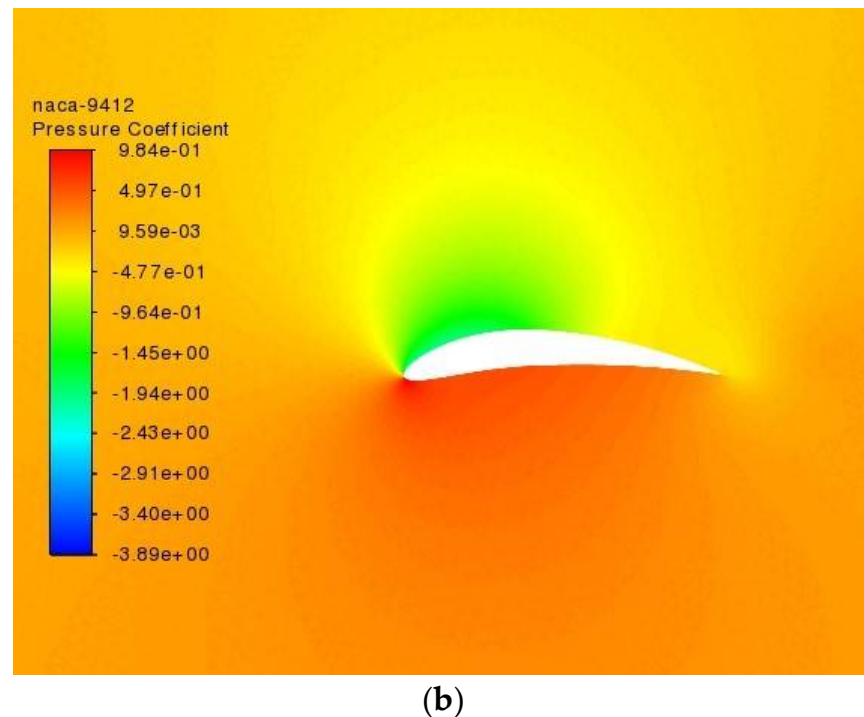


Figure 9. Cont.



**Figure 9.** Pressure contours of NACA 6412 at  $\alpha = 13^\circ$  (a) and NACA 9412 at  $\alpha = 11^\circ$  (b). ( $Re = 76,630$ ).

On the other hand, the conventional airfoils stall early. The stall angle corresponding to maximum  $C_L$  shifts to a lower value as the deflection angle increases. The highest value of stall angle obtained ( $\alpha = 11^\circ$ ) is for the airfoil configuration deflected  $1.5^\circ$ , which is the same  $\alpha$  for which the baseline airfoil stalls. Whereas all of the morphed airfoil configurations stall at  $\alpha \geq 11^\circ$ , none of the conventional airfoils stall at  $\alpha > 11^\circ$ . This implies that camber morphing wings would improve the manoeuvrability, agility, and stability of the aircraft. In fact, camber morphing wings flight-tested on a drone demonstrated the achievement of superior manoeuvrability by generating higher roll rates exclusively through morphing [27,31].

Amongst all cases, the greatest  $L$  is generated by NACA 9412 (9% camber rate) at  $\alpha = 11^\circ$ , which is only slightly greater than the  $L$  generated by the NACA 8412 airfoil for the same  $\alpha$ . Due to decreasing stall angles as the camber rate increases, the comparative enhancement in  $L$  with increasing camber rate starts to overlap and curb, starting at 6% camber rate at  $\alpha = 13^\circ$ . Overall, all configurations of morphed airfoils generate a greater  $C_L$  than the unmorphed baseline airfoils; morphing the camber by even 1% generates more  $L$ . Similarly, for the conventional airfoils, configurations deflected to a higher flap angle generate a greater maximum  $C_L$  value. There is a substantial leap in the maximum  $C_L$  value for two of the configurations shown in Figure 8, but this is due to the sharper increase of the deflection angle between the two configurations—from  $11.75^\circ$  to  $18.5^\circ$ . In an effort to match the increasing  $C_L$  values generated by the morphing airfoils at  $\alpha = 0^\circ$  by uniformly morphing the camber rate, the conventional airfoils need to deflect more to generate approximately similar  $C_L$  values.

For a comparative analysis of morphing and conventional airfoils, Figures 7 and 8 are plotted together and set forth in Figure 10. It is observed that the  $L$  profiles of morphed airfoils overlap with the  $L$  profiles generated by deflecting the flap angles of the conventional airfoils. Those configurations where the  $L$  profile of a morphing airfoil closely matches with the  $L$  profile of a conventional airfoil, or presents an approximately similar trend, was set as the basis of comparison. This region over which the  $L$  profiles match is called the “overlapping region”. These regions extend over a maximum of 10 angles (observed in the 1% camber-morphed and  $1.5^\circ$  flap-deflected case) to a minimum of 2 angles (observed in the 7% camber-morphed and  $11.5^\circ$  flap-deflected case). More information about the

matching cases, overlapping region, and corresponding morphing and conventional airfoil configurations is stated in Table 1.

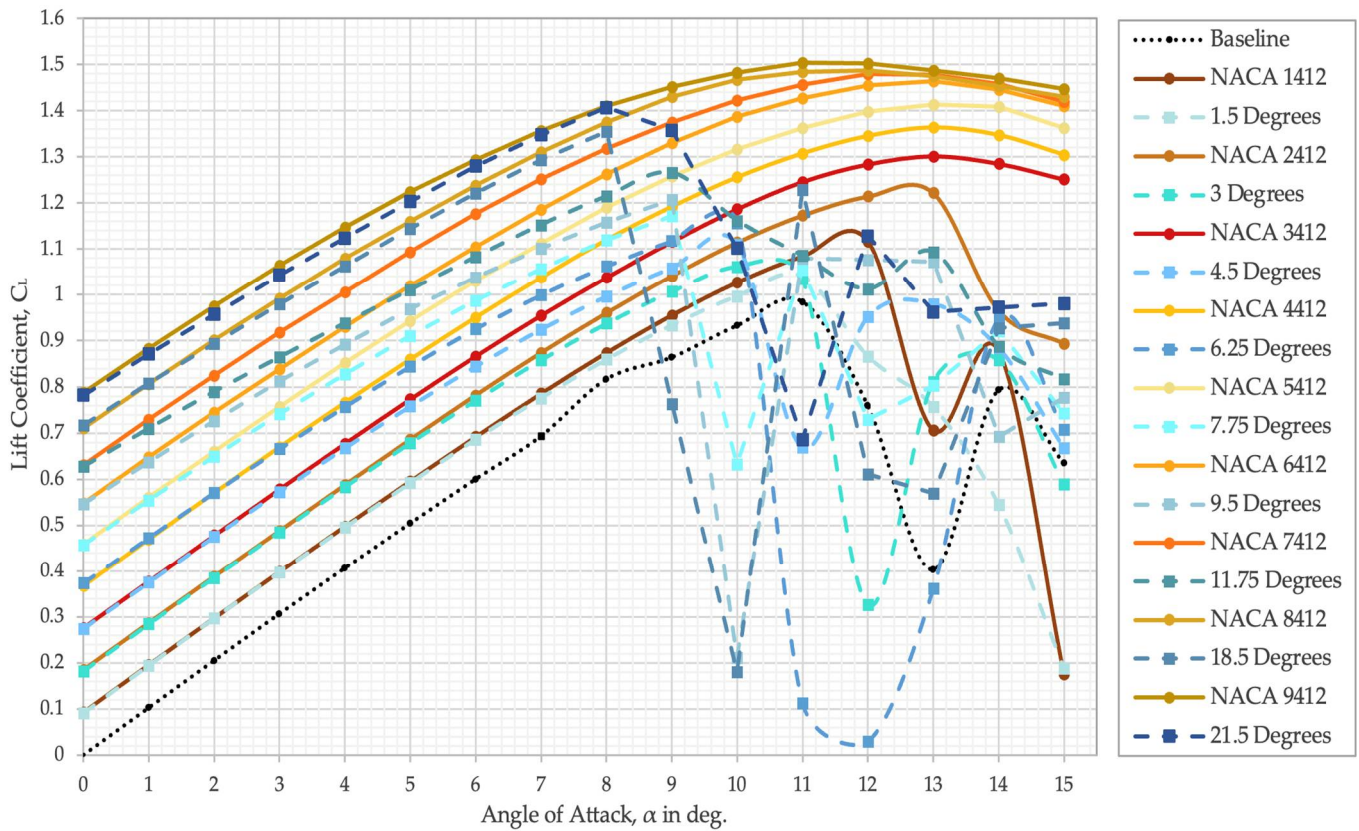
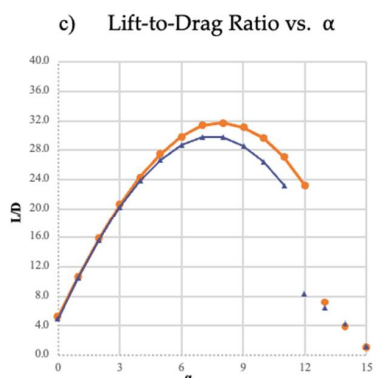
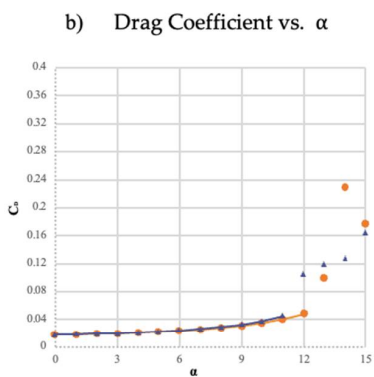
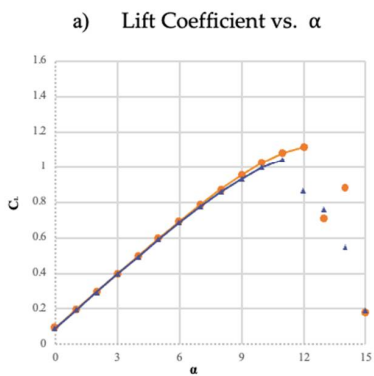
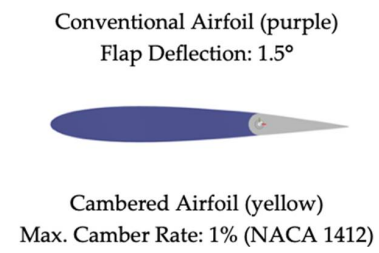


Figure 10. Overlapping lift plots of various morphing and deflecting airfoil configurations. ( $Re = 76,630$ ).

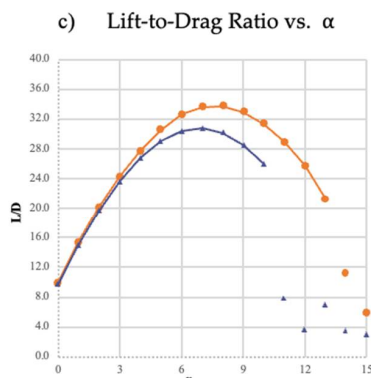
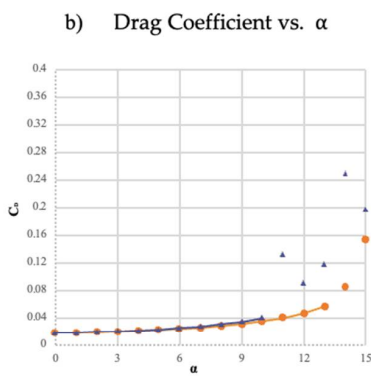
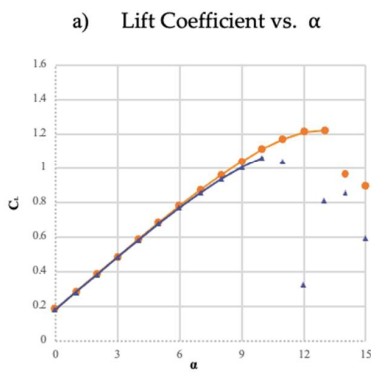
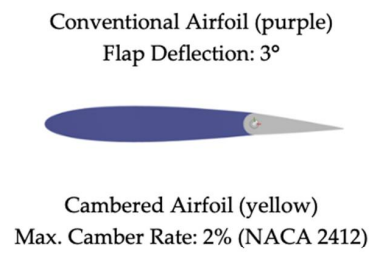
We were able to obtain matching cases for all morphing geometries considered. Morphing the camber rate by 1% generates the same amount of  $L$  as deflecting the flap angle by  $1.5^\circ$ . Similarly, morphing by 2% matches with flap deflection angle of  $3^\circ$ , and likewise all morphed configurations were matched with a configuration of conventional airfoil deflected to a certain flap angle. It is interesting to note that the overlapping region decreases for cases 1 to 7 but expands for case 8 and case 9 as depicted in Table 1.

Cases 1–9 were carefully identified after matching the  $L$  profiles of a camber-morphed airfoil configuration with a conventional airfoil deflected to a certain flap angle and results of the analysis of their aerodynamic parameters  $C_L$ ,  $C_D$ , and  $L/D$ , along with their geometric configurations are presented in Figure 11, where each column corresponds to one of the nine matching lift cases. From Figure 11A–C, the camber rate and the plain flap deflection angles are increasing (as shown in the geometric configurations in the first row) and the maximum  $C_L$  and  $C_D$  values also increase across each row.

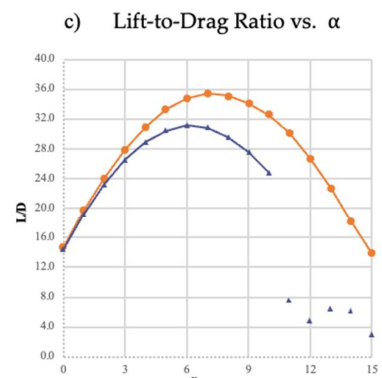
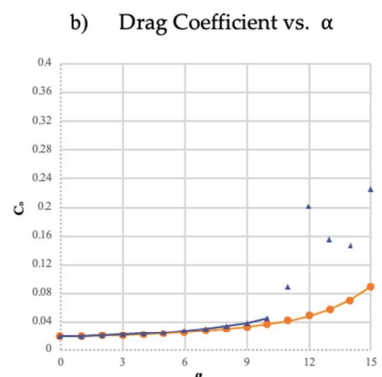
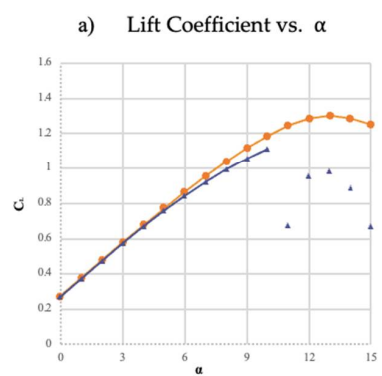
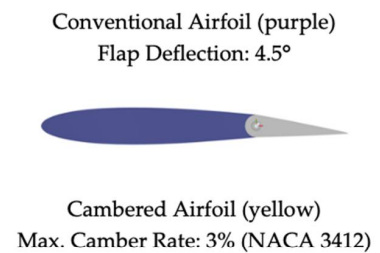
In all nine cases, the camber-morphed configurations generate lesser  $D$  than deflected angles in conventional airfoils. Cases 1, 2, 3, 8, and 9 present with the greatest overlapping regions but since conventional airfoils do not normally deflect to such high angles such as  $18^\circ$  or  $21^\circ$ , data from the first three cases are presented in Table 2 to validate the benefits of camber morphing. The  $L/D$  ratio was used as the comparison parameter because the aerodynamic efficiency of the aircraft is measured by its maximum  $L/D$  value. The ratio is also seen in calculations regarding the fuel efficiency and endurance of the aircraft [22] and is often set as the maximization factor in optimization studies.



At least 1.7% improvement in L/D if the camber is morphed by 1% instead of deflecting the flap 1.5°.



At least 1.8% improvement in the L/D if the camber is morphed by 2% instead of deflecting the flap 3°.



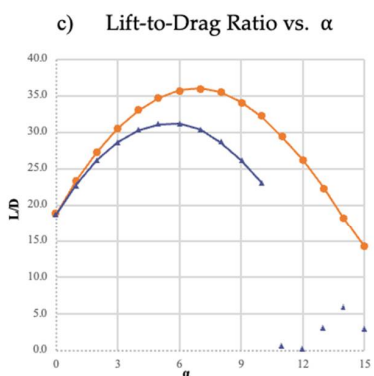
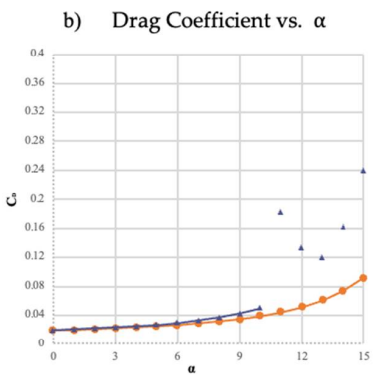
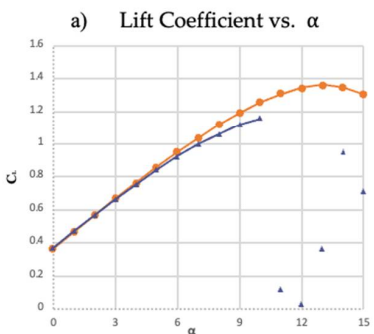
At least 1.7% improvement in the L/D if the camber is morphed by 3% instead of deflecting the flap 4.5°.

(A)

Figure 11. Cont.

Conventional Airfoil (purple)  
Flap Deflection: 6.25°

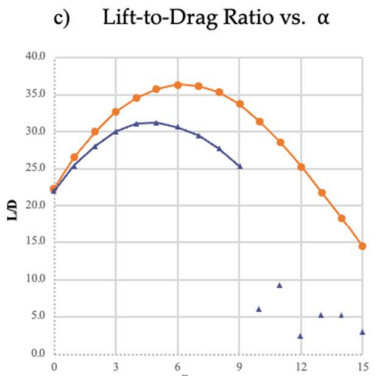
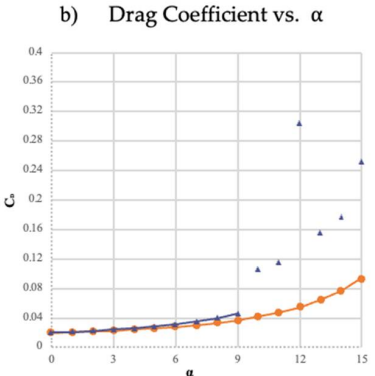
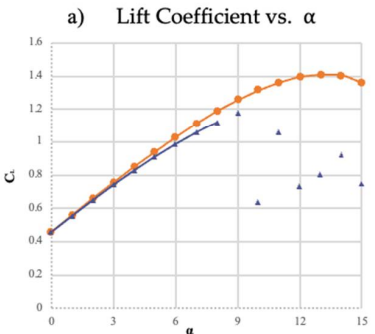
Cambered Airfoil (yellow)  
Max. Camber Rate: 4% (NACA 4412)



At least 0.24% improvement in the L/D if the camber is morphed by 4% instead of deflecting the flap 6.25°.

Conventional Airfoil (purple)  
Flap Deflection: 7.75°

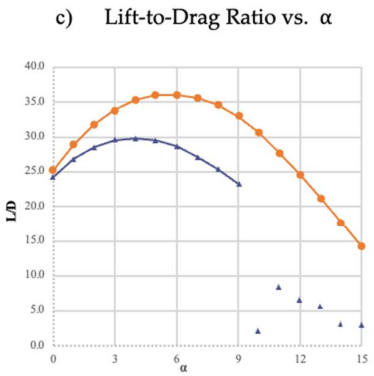
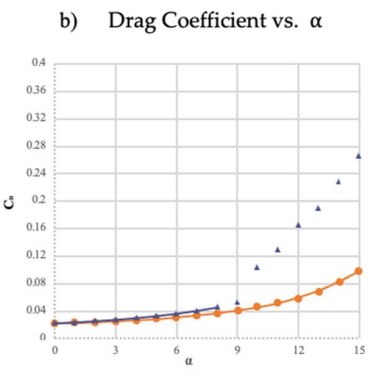
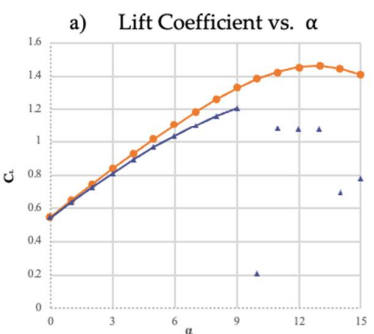
Cambered Airfoil (yellow)  
Max. Camber Rate: 5% (NACA 5412)



At least 1.6% improvement in the L/D if the camber is morphed by 5% instead of deflecting the flap 7.75°.

Conventional Airfoil (purple)  
Flap Deflection: 9.5°

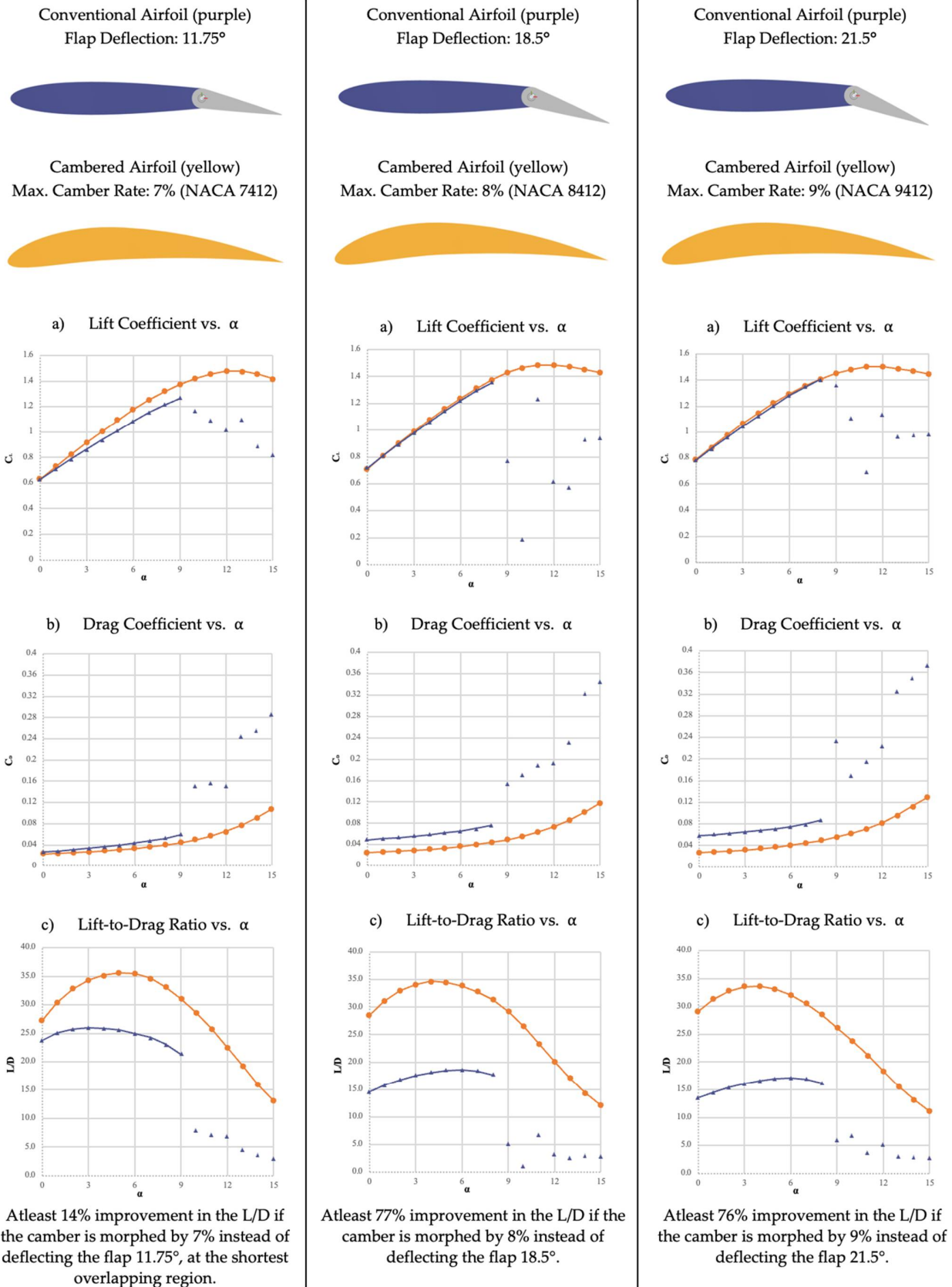
Cambered Airfoil (yellow)  
Max. Camber Rate: 6% (NACA 6412)



At least 3.9% improvement in the L/D if the camber is morphed by 6% instead of deflecting the flap 9.5°.

(B)

Figure 11. Cont.



(C)

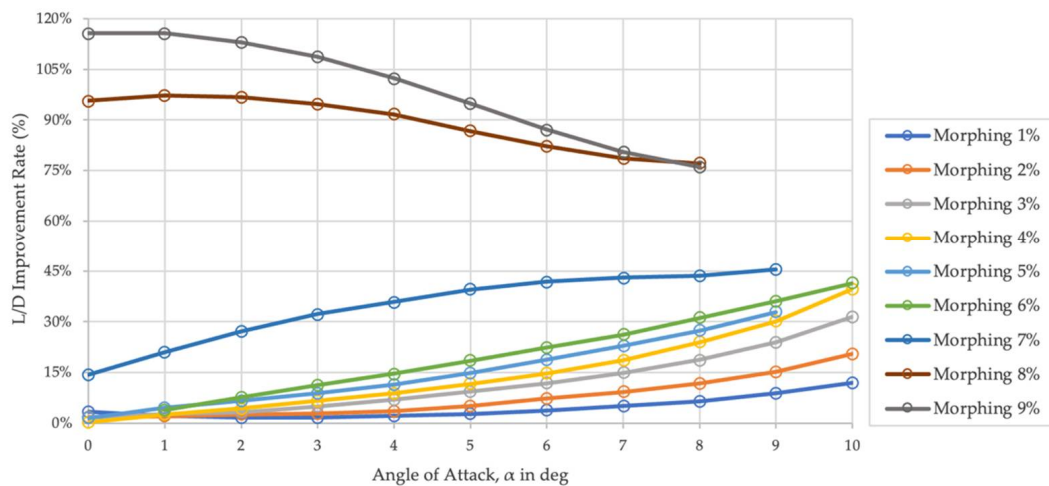
**Figure 11.** (A–C) Down each column, comparison of (a)  $C_L$ , (b)  $C_D$ , and (c) L/D of morphing (yellow) and conventional airfoils (purple).

**Table 2.** L/D of the matching cases and the percentage improvement in the L/D due to morphing.

$\alpha$	Percentage Improvement			Percentage Improvement			Percentage Improvement		
	NACA 1412	1.5°	Case 1	NACA 2412	3°	Case 2	NACA 3412	4.5°	Case 3
0	5.1	5.0	3.4%	10.0	9.8	1.8%	14.7	14.4	1.7%
1	10.7	10.5	2.2%	15.3	15.0	2.1%	19.7	19.2	2.8%
2	15.9	15.6	1.7%	20.2	19.7	2.5%	24.0	23.3	3.2%
3	20.5	20.1	1.7%	24.3	23.6	2.9%	27.9	26.6	4.9%
4	24.3	23.8	2.2%	27.8	26.9	3.5%	31.0	29.0	7.0%
5	27.4	26.7	2.8%	30.6	29.1	5.1%	33.3	30.5	9.4%
6	29.8	28.7	3.8%	32.6	30.4	7.3%	34.9	31.2	11.8%
7	31.3	29.8	5.1%	33.7	30.8	9.2%	35.5	30.9	14.9%
8	31.7	29.8	6.5%	33.8	30.2	11.8%	35.2	29.6	18.7%

In the overlapping region, on average, at least a 1.7% improvement in the *L/D* ratio can be expected for all cases. Outside the overlapping region, where the *L* generated is not approximately the same for both cases, cambered configurations generate more *L* and less *D*, thus improving the *L/D* ratio significantly. In addition, the morphing airfoils stall at a higher  $\alpha$  than the corresponding conventional airfoil which also improves the *L/D* tremendously. Though the percentage improvement for  $\alpha$  outside of the overlapping regions could have been ignored, it was included in Figure 12A,B for considering actual implementation and flight of morphing aircraft with given angles.

As shown in Figure 12A, NACA 7412 or a 7% camber-morphed airfoil shows a higher *L/D* improvement rate. However, it is noted from Table 2 that the NACA 7412 airfoil has the smallest overlapping region, so the improvement rate correlates to the fact that its corresponding conventional airfoil configuration generated lesser *L* and more *D* (as shown in Figure 11). The *L/D* improvement rate increases gradually as the camber rate increases in Figure 12B, and the greatest improvement can be expected when morphing with 7%, 8% or 9% camber rates. Consequently, the high values for the improvement rate in Figure 12 highlights the benefits of morphing. It is also implacable and meaningful to compare the *D* generated by different morphed and deflected configurations to visualize the reduction in drag due to morphing. Figures 13–15 show the *C<sub>D</sub>* plots that were cut off at the stall angle for better visualization. As seen in Figure 15, it is noteworthy that morphing the camber until the highest rate of 9%, still generates a lesser *D* than deflecting the flap 11.75° (which is the deflected configuration from case 7 that matches the *L* of the profile of the NACA 7412 airfoil).



(A)

**Figure 12.** Cont.

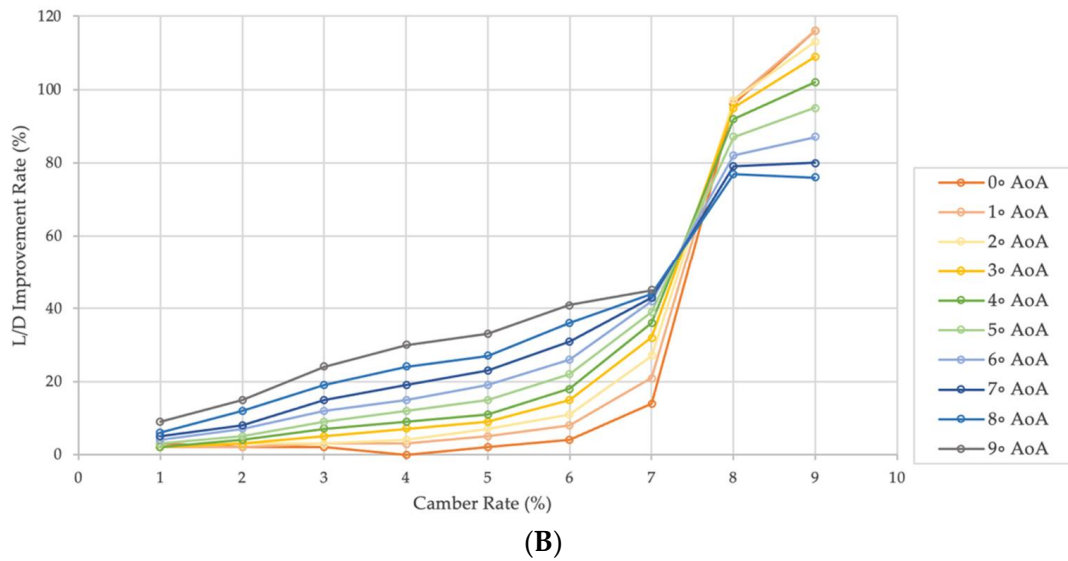


**Figure 12.** (A) Improvement in the L/D ratio when the camber is morphed instead of deflecting the flap. ( $Re = 76,630$ ). (B) Improvement in the L/D ratio as the camber rate is varied. ( $Re = 76,630$ ).

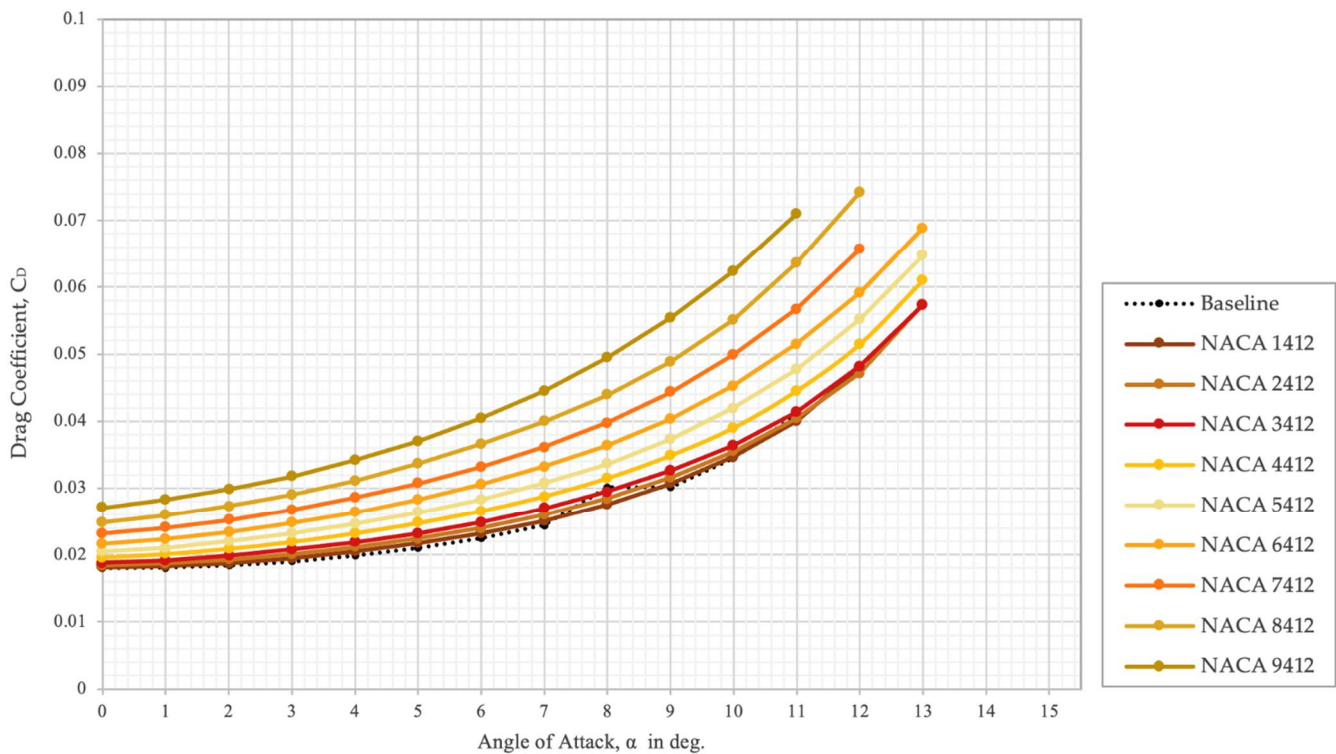


**Figure 13.** Morphing airfoils  $C_D$  plots, generated by varying the maximum camber rate. ( $Re = 76,630$ ).

An investigation of the behaviour of morphing wings at a low Reynolds number such as 76,630 is not a common practice, but small UAVs or MAVs—for which morphing wings are designed for—fly in flight conditions around this range so it is worthwhile to investigate the benefits of morphing in this flight condition. In the comparative analysis conducted between morphed and deflected airfoils, all morphed configurations output a better L/D ratio than the deflected configuration for every matching lift case studied.

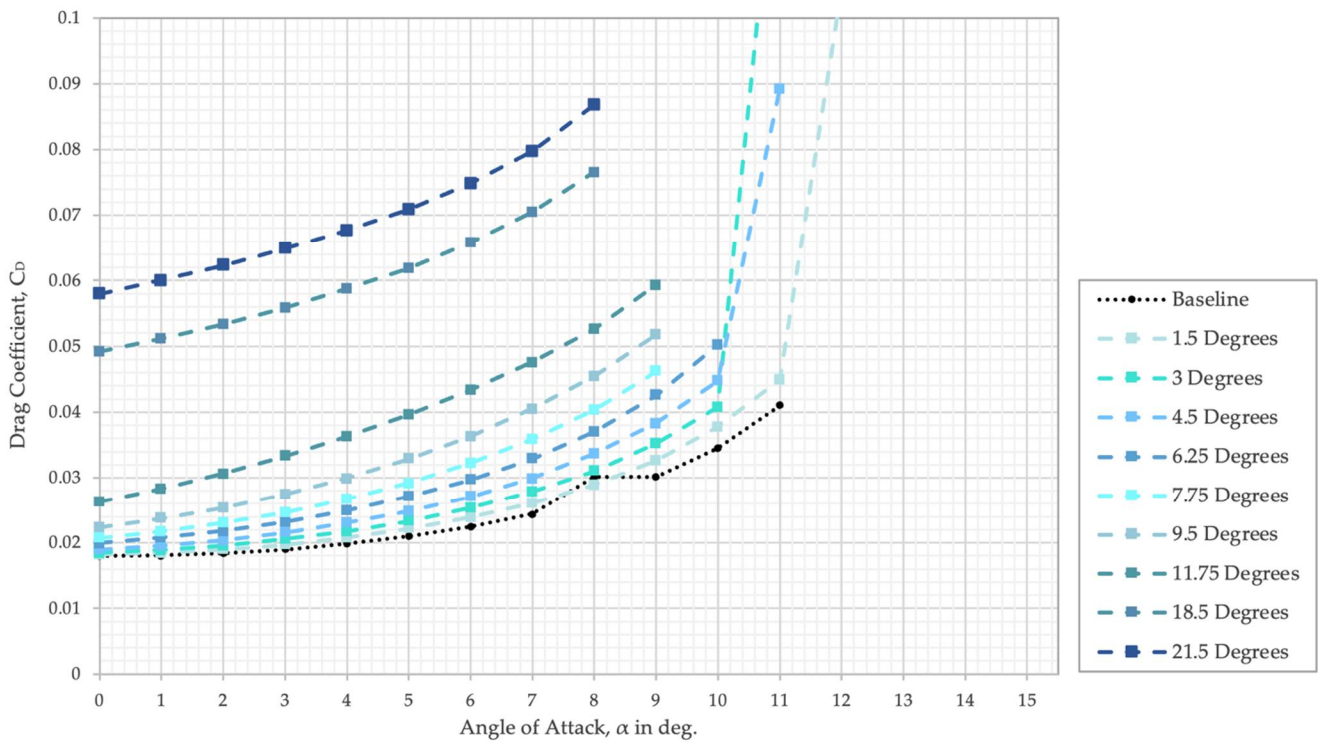


Figure 14. Conventional airfoils  $C_D$  plots, generated by varying the maximum camber rate. ( $Re = 76,630$ ).

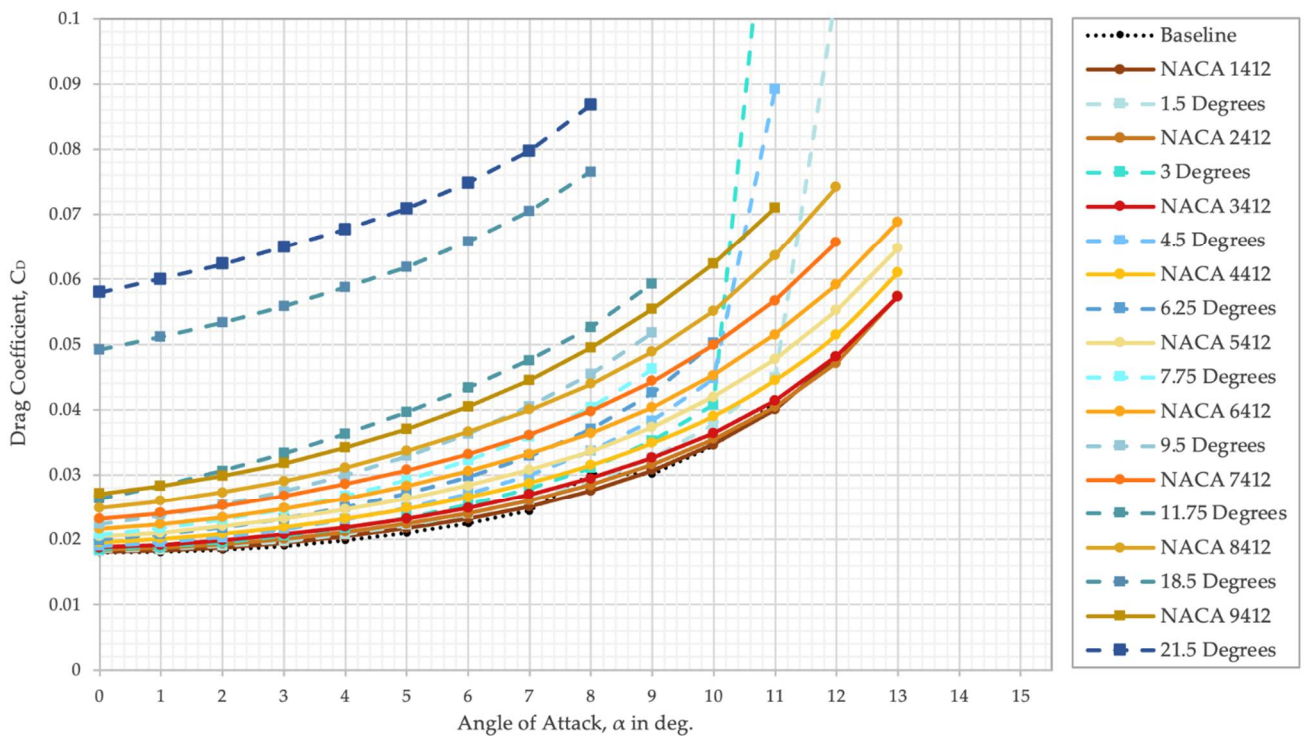


Figure 15. Overlapping  $C_D$  plots of various morphing and deflecting airfoil configurations. ( $Re = 76,630$ ).

### 5. Conclusions

This paper validates and highlights the aerodynamic benefits of a variable camber morphing wing using a computational method. A comparative numerical analysis has been conducted between 2D airfoils with a varying camber rate and a varying flap deflection angle—representing morphing wing and conventional wing scenarios. Particularly, the

authors emphasize that reducing  $D$ , while maintaining other aerodynamic parameters such as  $L$ , is directly related to  $L/D$ , the sustainability of aircraft operation and mission planning, and other parameters such as a higher stall angle improve the manoeuvrability and agility. Whereas all morphed configurations stall at an  $\alpha$  higher than the stall angle of the baseline configuration, none of the conventional airfoils (with any flap angle) generate a stall angle higher than that of the baseline configuration—implying that morphing the camber instead of employing a plain flap to change the shape of the baseline airfoil for improved manoeuvrability is advantageous. Furthermore, it has been found and validated that variable camber wings equivalent to conventional aircraft wings with varying deflection angles are improved in their  $L/D$  ratio in all nine cases considered, and up to 18.7% in case 3 at  $\alpha = 8^\circ$  with a 3% camber morphing rate. Overall, variable camber rate morphing wing, as one of the breakthrough technologies for next generation aircraft design, has been known for its innovative concept but not been fully validated for actual flight performance and mission planning. This paper established foundational works and addressed important aspects of the aerodynamic benefits of morphing compared to conventional wings in their  $L$ ,  $D$ , and  $L/D$  improvement.

**Author Contributions:** Conceptualization, B.W.J. and T.M.; methodology, B.W.J. and T.M.; software, T.M.; validation, T.M.; formal analysis, T.M.; investigation, B.W.J. and T.M.; data curation, T.M.; writing—original draft preparation, T.M. and B.W.J.; writing—review and editing, B.W.J. and T.M.; visualization, T.M.; supervision, B.W.J.; project administration, B.W.J.; funding acquisition, B.W.J. All authors have read and agreed to the published version of the manuscript.

**Funding:** This work is sponsored by InnoScience Co. Ltd. (20210901) and supported under the framework of the international cooperation program managed by the National Research Foundation (NRF) of Korea (NSFC 2021K2A9A2A06049018).

**Institutional Review Board Statement:** Not applicable.

**Informed Consent Statement:** Not applicable.

**Data Availability Statement:** Not applicable.

**Acknowledgments:** The authors greatly appreciate Air Force Research Laboratory (AFRL) Aerospace Directorate and Air Force Office of Scientific Research (AFOSR) for their research advice and information.

**Conflicts of Interest:** The authors declare no conflict of interest.

## Nomenclature

$L$	Lift force
$D$	Drag force
$\alpha$	Angle of attack
$C_L$	Lift coefficient
$C_D$	Drag coefficient
$y$	First layer thickness
$Re$	Reynolds number
$C_f$	Skin-friction coefficient
$\mu$	Dynamic viscosity
$\rho$	Air density
$v$	Air velocity
$\tilde{v}$	Spalart–Allmaras working variable

## Abbreviations

CFD	Computational fluid dynamics
CAD	Computer-aided design
$L/D$	Lift-to-drag ratio
RANS	Reynolds-averaged Navier–Stokes

S-A	Spalart–Allmaras
UAV	Unmanned aerial vehicle
MAV	Micro air vehicle
NACA	National Advisory Committee for Aeronautics

## References

- Barbarino, S.; Bilgen, O.; Ajaj, R.M.; Friswell, M.; Inman, D.J. A Review of Morphing Aircraft. *J. Intell. Mater. Syst. Struct.* **2011**, *22*, 823–877. [[CrossRef](#)]
- La, S.; Joe, W.Y.; Akbar, M.; Alsaidi, B. Surveys on skin design for morphing wing aircraft: Status and challenges. In Proceedings of the 2018 AIAA Aerospace Sciences Meeting, Kissimmee, FL, USA, 8–12 January 2018; p. 0315.
- Nordmann, A. Control Surfaces on Airfoil. Available online: [https://commons.wikimedia.org/wiki/File:Control\\_surfaces\\_on\\_airfoil.svg](https://commons.wikimedia.org/wiki/File:Control_surfaces_on_airfoil.svg) (accessed on 12 October 2012).
- Campanile, L.; Sachau, D. The belt-rib concept: A structronic approach to variable camber. *J. Intell. Mater. Syst. Struct.* **2000**, *11*, 215–224. [[CrossRef](#)]
- Keidel, D.; Sodja, J.; Werter, N.; de Breuker, R.; Ermanni, P. Development and testing of an unconventional morphing wing concept with variable chord and camber. In Proceedings of the 26th International Conference on Adaptive Structures and Technologies, Kobe, Japan, 25 October 2015; pp. 1–12.
- Zhang, P.; Zhou, L.; Cheng, W.; Qiu, T. Conceptual Design and Experimental Demonstration of a Distributedly Actuated Morphing Wing. *J. Aircr.* **2015**, *52*, 452–461. [[CrossRef](#)]
- Li, H.; Liu, L.; Xiao, T.; Ang, H. Design and simulative experiment of an innovative trailing edge morphing mechanism driven by artificial muscles embedded in skin. *Smart Mater. Struct.* **2016**, *25*, 095004. [[CrossRef](#)]
- Molinari, G.; Quack, M.; Arrieta, A.F.; Morari, M.; Ermanni, P. Design, realization and structural testing of a compliant adaptable wing. *Smart Mater. Struct.* **2015**, *24*, 105027. [[CrossRef](#)]
- Maki, M. Experimental Study of a Morphing Wing Configuration with Multi-Slotted Variable-Camber Mechanism. In Proceedings of the AIAA Atmospheric Flight Mechanics Conference, Washington, DC, USA, 13–17 June 2016; p. 3849.
- Maute, K.; Reich, G.W. Integrated Multidisciplinary Topology Optimization Approach to Adaptive Wing Design. *J. Aircr.* **2006**, *43*, 253–263. [[CrossRef](#)]
- Sun, J.; Guan, Q.; Liu, Y.; Leng, J. Morphing aircraft based on smart materials and structures: A state-of-the-art review. *J. Intell. Mater. Syst. Struct.* **2016**, *27*, 2289–2312. [[CrossRef](#)]
- Li, D.; Zhao, S.; Da Ronch, A.; Xiang, J.; Drofelnik, J.; Li, Y.; Zhang, L.; Wu, Y.; Kintscher, M.; Monner, H.P.; et al. A review of modelling and analysis of morphing wings. *Prog. Aerosp. Sci.* **2018**, *100*, 46–62. [[CrossRef](#)]
- Dhileep, K.; Kumar, D.; Ghosh, S.; Faruque Ali, S. Numerical Study of Camber Morphing in NACA0012 Airfoil. In Proceedings of the AIAA AVIATION 2020 FORUM, Online, 15–19 June 2020; p. 2781.
- Kumar, D.; Ali, S.F.; Arockiarajan, A. Structural and Aerodynamics Studies on Various Wing Configurations for Morphing. *IFAC-PapersOnLine* **2018**, *51*, 498–503. [[CrossRef](#)]
- Zhang, J.; Shaw, A.D.; Wang, C.; Gu, H.; Amoozgar, M.; Friswell, M.I.; Woods, B.K. Aeroelastic model and analysis of an active camber morphing wing. *Aerosp. Sci. Technol.* **2021**, *111*, 106534. [[CrossRef](#)]
- Bishay, P.L.; Finden, R.; Recinos, S.; Alas, C.; Lopez, E.; Aslanpour, D.; Flores, D.; Gonzalez, E. Development of an SMA-based camber morphing UAV tail core design. *Smart Mater. Struct.* **2019**, *28*, 075024. [[CrossRef](#)]
- Kang, W.-R.; Kim, E.-H.; Jeong, M.-S.; Lee, I.; Ahn, S.-M. Morphing Wing Mechanism Using an SMA Wire Actuator. *Int. J. Aeronaut. Space Sci.* **2012**, *13*, 58–63. [[CrossRef](#)]
- Basaeri, H.; Yousefi-Koma, A.; Zakerzadeh, M.R.; Mohtasebi, S.S. Experimental study of a bio-inspired robotic morphing wing mechanism actuated by shape memory alloy wires. *Mechatronics* **2014**, *24*, 1231–1241. [[CrossRef](#)]
- Yokozeki, T.; Sugiura, A.; Hirano, Y. Development of Variable Camber Morphing Airfoil Using Corrugated Structure. *J. Aircr.* **2014**, *51*, 1023–1029. [[CrossRef](#)]
- Meguid, S.A.; Su, Y.; Wang, Y. Complete morphing wing design using flexible-rib system. *Int. J. Mech. Mater. Des.* **2017**, *13*, 159–171. [[CrossRef](#)]
- Communier, D.; Botez, R.M.; Wong, T. Design and Validation of a New Morphing Camber System by Testing in the Price—Païdoussis Subsonic Wind Tunnel. *Aerospace* **2020**, *7*, 23. [[CrossRef](#)]
- Wu, R.; Soutis, C.; Zhong, S.; Filippone, A. A morphing aerofoil with highly controllable aerodynamic performance. *Aeronaut. J.* **2017**, *121*, 54–72. [[CrossRef](#)]
- Vasista, S.; Tong, L. Topology-Optimized Design and Testing of a Pressure-Driven Morphing-Aerofoil Trailing-Edge Structure. *AIAA J.* **2013**, *51*, 1898–1907. [[CrossRef](#)]
- Meyer, P.; Lück, S.; Spuhler, T.; Bode, C.; Hühne, C.; Friedrichs, J.; Sinapius, M. Transient Dynamic System Behavior of Pressure Actuated Cellular Structures in a Morphing Wing. *Aerospace* **2021**, *8*, 89. [[CrossRef](#)]
- Woods, B.K.; Bilgen, O.; Friswell, M. Wind tunnel testing of the fish bone active camber morphing concept. *J. Intell. Mater. Syst. Struct.* **2014**, *25*, 772–785. [[CrossRef](#)]
- Zhang, Y.; Ge, W.; Zhang, Z.; Mo, X.; Zhang, Y. Design of compliant mechanism-based variable camber morphing wing with nonlinear large deformation. *Int. J. Adv. Robot. Syst.* **2019**, *16*, 1729881419886740. [[CrossRef](#)]

27. Molinari, G.; Arrieta, A.F.; Guillaume, M.; Ermanni, P. Aerostructural Performance of Distributed Compliance Morphing Wings: Wind Tunnel and Flight Testing. *AIAA J.* **2016**, *54*, 3859–3871. [[CrossRef](#)]
28. Chanzy, Q.; Keane, A. Analysis and experimental validation of morphing UAV wings. *Aeronaut. J.* **2018**, *122*, 390–408. [[CrossRef](#)]
29. Keidel, D.; Fasel, U.; Molinari, G.; Ermanni, P. Design, Development, and Structural Testing of a Camber-Morphing Flying Wing Airplane. In *Smart Materials, Adaptive Structures and Intelligent Systems*; American Society of Mechanical Engineers: New York, NY, USA, 2017; Volume 58264, p. V002T04A013.
30. Zhao, A.; Zou, H.; Jin, H.; Wen, D. Structural design and verification of an innovative whole adaptive variable camber wing. *Aerosp. Sci. Technol.* **2019**, *89*, 11–18. [[CrossRef](#)]
31. Fasel, U.; Keidel, D.; Baumann, L.; Cavolina, G.; Eichenhofer, M.; Ermanni, P. Composite additive manufacturing of morphing aerospace structures. *Manuf. Lett.* **2020**, *23*, 85–88. [[CrossRef](#)]
32. Alsulami, A.; Akbar, M.; Joe, W.Y. A Comparative Study: Aerodynamics of Morphed Airfoils Using CFD Techniques and Analytical Tools. In *ASME International Mechanical Engineering Congress and Exposition*; American Society of Mechanical Engineers: New York, NY, USA, 2017; Volume 58349, p. V001T03A010.
33. Cheung, K.; Cellucci, D.; Copplestone, G.; Cramer, N.; Fusco, J.; Jenett, B.; Kim, J.; Langford, A.; Mazhari, A.; Trinh, G.; et al. Development of Mission Adaptive Digital Composite Aerostructure Technologies (MADCAT). In Proceedings of the 17th AIAA Aviation Technology, Integration, and Operations Conference, Denver, CO, USA, 5–9 June 2017; p. 4273.
34. Kudva, J.N. Overview of the DARPA Smart Wing Project. *J. Intell. Mater. Syst. Struct.* **2004**, *15*, 261–267. [[CrossRef](#)]
35. Kota, S.; Osborn, R.; Ervin, G.; Maric, D.; Flick, P.; Paul, D. Mission adaptive compliant wing—design, fabrication and flight test. In *RTO Applied Vehicle Technology Panel (AVT) Symposium*; RTO-MP-AVT-168; NATO-OTAN: Evora, Portugal, 2009; p. 18-1.
36. Vasista, S.; Riemenschneider, J.; Van De Kamp, B.; Monner, H.P.; Cheung, R.C.M.; Wales, C.; Cooper, J.E. Evaluation of a Compliant Droop-Nose Morphing Wing Tip via Experimental Tests. *J. Aircr.* **2017**, *54*, 519–534. [[CrossRef](#)]
37. Nguyen, N.; Lebofsky, S.; Ting, E.; Kaul, U.; Chaparro, D.; Urnes, J. Development of Variable Camber Continuous Trailing Edge Flap for Performance Adaptive Aeroelastic Wing. In *SAE AeroTech Congress & Exhibition*; SAE International: Washington, DC, USA, 2015.
38. Kumar, T.R.S.; Venugopal, S.; Ramakrishnananda, B.; Vijay, S. Aerodynamic Performance Estimation of Camber Morphing Airfoils for Small Unmanned Aerial Vehicle. *J. Aerosp. Technol. Manag.* **2020**, *12*, 1420. [[CrossRef](#)]
39. Huntley, S.J.; Woods, B.K.; Allen, C.B. Computational Analysis of the Aerodynamics of Camber Morphing. In Proceedings of the AIAA Aviation 2019 Forum, Dallas, TX, USA, 17–21 June 2019; p. 2914.
40. Alulema, V.H.; Valencia, E.; Pillajo, D.; Jacome, M.; Lopez, J.; Ayala, B. Degree of Deformation and Power Consumption of Compliant and Rigid-linked Mechanisms for Variable-Camber Morphing Wing UAVs. In Proceedings of the AIAA Propulsion and Energy 2020 Forum, Virtual Event, 24–28 August 2020; p. 3958.
41. Taguchi, K.; Fukunishi, K.; Takazawa, S.; Sunada, Y.; Imamura, T.; Rinoie, K.; Yokozeki, T. Experimental Study about the Deformation and Aerodynamic Characteristics of the Passive Morphing Airfoil. *Trans. Jpn. Soc. Aeronaut. Space Sci.* **2020**, *63*, 18–23. [[CrossRef](#)]
42. Spalart, P.; Allmaras, S. A one-equation turbulence model for aerodynamic flows. In Proceedings of the 30th Aerospace Sciences Meeting and Exhibit, Reno, NV, USA, 6–9 January 1992; p. 439.
43. Goetten, F.; Finger, D.; Marino, M.; Bil, C.; Havermann, M.; Braun, C. A review of guidelines and best practices for subsonic aerodynamic simulations using RANS CFD. In *APISAT 2019: Asia Pacific International Symposium on Aerospace Technology*; Engineers Gold Coast: Burleigh Heads, QLD, Australia, 2019; p. 227.
44. Schlichting, H.; Kestin, J. *Boundary Layer Theory*; Springer: Berlin/Heidelberg, Germany, 1961.
45. Ladson, C.L. *Effects of Independent Variation of Mach and Reynolds Numbers on the Low-Speed Aerodynamic Characteristics of the NACA 0012 Airfoil Section*; National Aeronautics and Space Administration, Scientific and Technical Information Division: Washington, DC, USA, 1988.
46. 2D NACA 0012 Airfoil Validation Case. Available online: [https://turbmodels.larc.nasa.gov/naca0012numerics\\_val.html](https://turbmodels.larc.nasa.gov/naca0012numerics_val.html) (accessed on 20 October 2021).
47. Airfoil Tools. Available online: <http://airfoiltools.com/airfoil/naca4digit> (accessed on 20 October 2021).
48. Ohtake, T.; Nakae, Y.; Motohashi, T. Nonlinearity of the aerodynamic characteristics of NACA0012 aerofoil at low Reynolds numbers. *Jpn. Soc. Aeronaut. Space Sci.* **2007**, *55*, 439–445.